MTLA 35 (2024) 102111

Contents lists available at ScienceDirect

Materialia

journal homepage: www.elsevier.com/locate/mtla

Relating laser powder bed fusion process parameters to (micro)structure and to soft magnetic behaviour in a Fe-based bulk metallic glass

M. Rodríguez-Sánchez [a,b,*], S. Sadanand [a,b], A. Ghavimi [c], R. Busch [c], P. Tiberto [d], E. Ferrara [d], G. Barrera [d], L. Thorsson [e], H.J. Wachter [e], I. Gallino [c,f], M.T. Pérez-Prado [a]

[a] IMDEA Materials Institute, Calle Eric Kandel, 2, Getafe, Madrid 28906, Spain
[b] Materials Science and Engineering Department, Universidad Carlos III de Madrid, Av. De la Universidad 30, Leganés, Madrid 28911, Spain
[c] Saarland University, Institute of Metallic Materials, Campus C6.3 66123, Saarbrücken, Germany
[d] INRIM, Istituto Nazionale di Ricerca Metrologica, Strade delle Cacce, 5, Torino 10135, Italy
[e] Hereaus AMLOY Technologies GmbH, Seligenstädter Straße 100, Karlstein 63791, Germany
[f] Technical University of Berlin, Department of Materials Science and Engineering, Metallic Materials, Ernst-Reuter Platz 1, Berlin 10587, Germany

ARTICLE INFO

Keywords:
Bulk metallic glasses
Soft magnetic materials
Laser powder bed fusion
Kuamet

ABSTRACT

This work aims to establish fundamental processing-(micro)structure-property links in a commercial Fe-based Kuamet6B2 bulk metallic glass (BMG) processed by laser powder bed fusion (LPBF). With that purpose, amorphous powders were processed using a pulsed-wave system and a simple meander strategy. The laser power, the scan speed, and the hatch distance were varied over wide intervals within the conduction regime. The processability window leading to samples with good dimensional accuracy and mechanical stability was determined. Within this window, the manufactured samples were crystalline/amorphous composites and the crystalline regions were formed by equiaxed ultrafine and nanograins with random orientations. Processing parameters yielding the densest prints caused severe crystallization while, conversely, parameter sets allowing the material to retain a high amorphous fraction led to significant lack-of-fusion defects and residual cracking along directions perpendicular to crystalline/amorphous interfaces. Comparatively, for a fixed hatch distance, the scanning speed had a stronger effect than the laser power in the resulting amorphous fraction due to its stronger influence on the melt pool size and, in turn, on the corresponding HAZ volume. The saturation magnetization and the coercive field were inversely related to the amorphous fraction. This work allows to derive fundamental guidelines for the successful additive manufacturing of soft magnetic Fe-based bulk metallic glasses (BMGs) by laser powder bed fusion (LPBF).

1. Introduction

As part of the global goal to reduce greenhouse gas emissions, emphasis has been placed on the replacement of combustion engines for electric motors in the transportation sector. To deliver a quick response when an alternating current (AC) is applied, the electro-magnetic devices in such increasingly demanded motors use soft magnetic materials (SMMs), which are characterized by having low coercivity (H_c), high permeability (μ_s), and high saturation magnetization (M_s) per unit mass [1]. Fe-based bulk metallic glasses (BMGs) exhibit excellent soft magnetic behaviour due to their disordered atomic structure and to the corresponding lack of grains or grain boundaries [2,3]. Such structure is retained when the molten metal is solidified by rapid cooling methods at rates of approximately 10^5 - 10^6 K/s, depending on the alloy composition [4]. However, the glass forming ability (GFA) of Fe-based BMGs is relatively low and, thus, the manufacturing routes for this family of materials are typically limited to melt spinning to produce thin ribbons [5], to suction casting of thin rods [6] or plates [7], and to powder atomization [8]. Ultimately, the impossibility to manufacture large-scale soft magnetic components of complex geometries with amorphous structure constitutes a major barrier limiting the practical application of Fe-based BMGs.

Powder-based additive manufacturing (AM) methods, such as laser powder bed fusion (LPBF), offer the possibility to fabricate components with intricate geometries from selected feedstock powder. The laser in LPBF machines has in general a small spot size and melts only a small

* Corresponding author.
E-mail address: marcos.rodriguez@imdea.org (M. Rodríguez-Sánchez).

https://doi.org/10.1016/j.mtla.2024.102111
Received 25 April 2024; Accepted 1 May 2024
Available online 2 May 2024

volume of powder as it scans each layer, achieving high local cooling rates approaching 10^5 – 10^7 K/s [9-12], i.e., including the orders of magnitude required to fabricate metallic glasses in their fully amorphous form. Therefore, LPBF constitutes a suitable avenue to overcome the size and geometry limitations associated with BMG processing and has already been used on different alloy systems for an array of applications [13-19]. It is widely recognized [20] that AM has limitations, including the generation of residual stresses and internal defects, which can impact the final part's quality. Additionally, the heat affected zone (HAZ) originated in the vicinity of each melt pool may extend to the layers located immediately below the one that is being melted, resulting often in undesired devitrification [14,21,22]. Nevertheless, BMG systems with high GFA such as Zr-based alloys have been successfully manufactured with LPBF, typically reaching high relative densities (> 99.5%) in components with fully amorphous structures, or occasionally with minimal degrees of crystallization [23-27].

Due to their comparatively small GFA, AM of Fe-based BMGs has remained challenging [16]. A number of studies in the literature have presented the results of LPBF processing trials on different Fe-based systems in the last decade [28-46]. Some have tested extensive and complex processing parameter optimization methods to maximize the relative part density and to minimize crystallization [21,28,33,38,44,45]. It has been shown that LPBF parameter combinations involving high-energy inputs result in dense samples but favour crystallization, while low-energy parameter combinations promote the retention of the amorphous phase. Hence, Fe-based alloys processed with LPBF generally exhibit composite structures including both crystalline and amorphous regions. Crystallization during LPBF severely compromises the soft magnetic behaviour of Fe-based BMGs as grain growth leads to an increase in the coercivity and to a decrease of the permeability, despite having a moderate positive influence on saturation magnetisation [3]. Several studies [28,42,45] have reported that partially crystalline LPBF-processed samples of different Fe-based BMGs exhibit coercive fields that are several orders of magnitude higher than what is typically expected from fully amorphous ribbons with the same composition. Hence, attempting to maximize simultaneously the mechanical integrity and the soft magnetic behaviour of LPBF manufactured components of these materials necessarily requires devising innovative methods to minimize crystallization during processing.

The Fe-Si-B-Cr-C system has drawn special interest for its remarkable soft magnetic behaviour, the relatively large availability of its elements and the absence of rare earth or highly demanded elements, such as Co. To date there is very limited information regarding the LPBF processability of this alloy class, as only a handful of studies have been published on this topic [45,47-50]. Furthermore, these studies utilize different alloy compositions within the Fe-Si-B-Cr-C system, as well as various LPBF machines, and thus it is not straightforward to extract basic processing-structure-property relations that can be transferred to a wide range of alloy/machine combinations. In the most successful cases, complex scanning strategies favouring heat dissipation such as the double-scanning strategy reported by Nam et al. [49] or the point-random scanning strategy proposed by Zrodowski et al. [47], are utilized to maximize, simultaneously, the component density and the fraction of amorphous phase. Some of these approaches have yielded promising results at the expense of increased build times [48]. However, the large number of LPBF parameters to be optimized, which are often not fully disclosed, as well as the limited information regarding the crystalline/amorphous composite structures formed, together with the complexity of the scan strategies proposed, obscure the fundamental knowledge underlying LPBF processing of the mentioned Fe-based BMG alloys.

The aim of this work is to build a solid relationship between the LPBF processing parameters, the corresponding (micro)structure and the magnetic properties of the commercial Fe-based Kuamet6B2 BMG alloy using a simple scanning strategy. With that goal, the material under investigation was additively manufactured with a pulsed-wave LPBF system using a wide array of process parameter combinations and a meander scanning strategy. In particular, critical processing parameters, including the laser power, the scan speed, and the hatch distance were varied over a large range of values. Several complementary characterization techniques were then utilized to assess the defect structure, the fraction of amorphous material, and the (micro)structure of the crystalline regions of the printed parts. The latter was then related to the corresponding magnetic properties, including the saturation magnetization and the coercivity. The associated electrical losses are also discussed. This study aims to provide guidelines to leverage LPBF AM methods to produce soft magnetic Fe-based BMG components.

2. Materials and methods

The commercial powder used in this work is known as Kuamet6B2 ($Fe_{73.7}B_{11}Si_{11}Cr_{2.3}C_2$ [at.%]) and it was produced by Epson Atmix by means of spinning water atomization [7]. The powder was handled and stored in small containers while working in a glovebox with an argon atmosphere to limit oxidation. Prior to LPBF processing, the morphology of the feedstock powder particles was evaluated by field emission gun scanning electron microscopy (FEGSEM) using an Apreo 2S (ThermoFisher Scientific) system. As illustrated on Fig. 1, most particles exhibited good spheroidicity and almost no satellites were found. The rheological properties of the powder were measured using standard ASTM methods (ASTM B213 [51] and ASTM B527 [52]). The Hall flowability (23.4 s) was calculated as an average of three tests, during which the powders were observed to flow uninterruptedly through the flowmeter. The powder's apparent (ρ_a) and tapped (ρ_t) densities were 4.0 and 4.3 g/cm^3, respectively. From these density measurements, the Carr Index ($CI = (\rho_t - \rho_a)/\rho_t$) and the Hausner Ratio ($HR = \rho_t/\rho_a$), which are also indicators of powder flowability [53], were calculated. The CI and HR values of the powder used in this study, which are compared with reference values in Table 1, suggest excellent flowability. The particle size distribution, which was measured using a Bettersize laser particle size analyser, is characterized by the following metrics: D_{10} = 11 μm, D_{50} = 30 μm, and D_{90} = 61 μm. X-ray diffraction (XRD) was carried out in a Malvern PANalytical Empyrean X-ray diffractometer using Cu Kα radiation to evaluate qualitatively the phase distribution of the powder particles. A melt-spun ribbon was used as a benchmark. Also, a Perkin Elmer DSC8000 differential scanning calorimeter (DSC) was utilized to quantify the amorphous fraction, which was calculated from the ratio of the crystallization enthalpy of the sample to that of a melt-spun ribbon of the same composition ($AM\% = \Delta H_{cr,sample}/\Delta H_{cr,ribbon}$). The amorphous fraction of the feedstock powder amounted to 82%.

The LPBF system used in this work was a Renishaw AM400. This system uses a 400 W pulsed-wave ytterbium fibre laser with a spot size of 70 μm. A reduced build volume (RBV) platform furnished with a 316 L

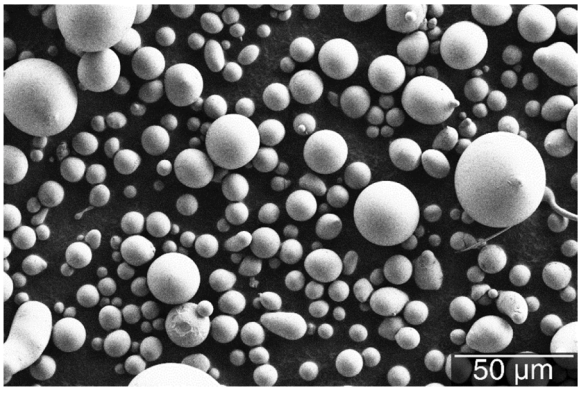

Fig. 1. SEM micrograph illustrating the spinning water-atomized Kuamet6B2 powder. The image was obtained using the secondary electron (SE) signal.

Table 1
Comparison of Kuamet6B2 powder flow properties (Carr Index, CI and Hausner Ratio, HR) with reference values [15].

Flow Character	CI	HR
Poor	>25	>1.34
Passable	20–25	1.25–1.35
Fair	15–20	1.18–1.11
Good	10–15	1.11–1.18
Excellent	0–10	1–1.11
Kuamet6B2 (This study)	**5.62**	**1.06**

steel substrate was utilized to minimize powder waste and simple prism samples of 8 × 8 × 9.5 mm^3 in size were fabricated in two different printing campaigns to study the relationship between the processing parameters, the generated (micro)structure and the corresponding soft magnetic properties. The selected scanning strategy was always meander (also known as zig-zag or bidirectional), with a rotation in the scanning direction of 67° between subsequent layers. The first LPBF processing campaign (Print 1) was aimed at studying the influence of the laser power (P) and scan speed (v) while all other parameters were kept constant. The hatch distance (h) was fixed at 80 μm and the layer thickness (t) at 30 μm (equivalent to the D_{50} particle size). P was varied between 20 and 60 W. Due to the pulsed nature of the laser, v can be modified by changing the exposure time (t_{exp}) and/or the point distance (pd), as which are related by the expression $v = pd/(10 + t_{exp})$. In the present work, pd was fixed at 80 μm while t_{exp} was tuned to vary v between 350 and 650 mm/s. The processing parameter combinations probed in Print 1 are depicted in Fig. 2(a) and are summarized in Table 2. A total of 14 LPBF parameter sets (samples KS1-KS14) were explored. The volumetric energy density ($VED = P/(vth)$) is also included in Table 2 for reference. The second LPBF processing campaign (Print 2) was aimed at investigating the influence of h. In particular, four parameter sets including the extreme P and v values of Print 1 (KS1 (20 W, 350 mm/s, VED=23 J/mm^3), KS3 (20 W, 650 mm/s, VED=12 J/mm^3), KS11 (50 W, 350 mm/s, VED=59 J/mm^3), and KS13 (50 W, 650 mm/s, VED=32 J/mm^3)), were selected, and, for each of them, h was varied between 50, 70, and 90 μm. Since KS3 lead to a combination of extremely low VED, the highest h value (90 μm) was not attempted on this combination of parameters. Fig. 2 (b-d) depicts the parameter sets that were probed in Print 2, which are also summarized in Table 2. A total of 11 LPBF parameter combinations (KS15-KS25) were tested in the second campaign.

The LPBF manufactured Kuamet6B2 samples were first removed from the substrate plate and then they were sectioned along the build direction (BD) with a Struers Secotom-20 disc cutting machine. The surface of half of the cut samples was ground and polished for defect analysis. Diamond pastes of decreasing particle sizes (down to 1/4 μm) and a 0.04 μm colloidal silica polishing suspension were used for optimal surface finish. An Olympus BX51 optical microscope was then used to image the mirror-polished cross sections. The relative density of each print could be roughly estimated from the optical micrographs using the image analysis software ImageJ/Fiji by thresholding and binarizing the images, a method that is widely reported in the literature [54-56]. The density values corresponding to the samples manufactured within prints 1 and 2 are summarized in Table 2. Next, Fiji's machine learning-assisted segmentation plug-in, the WEKA trainable segmentation package [57], was used to segment representative optical micrographs (Fig. 3a) into binarized images of voids (Fig. 3b) and cracks (Fig. 3c), respectively. Voids were indexed via a particle analyser plug-in and later filtered based on size. Filtering was done by setting an area threshold of 2500 pixels, which allowed to isolate small circular pores resulting from keyhole effects and from trapped gas (hereafter named "small pores") from large and irregularly shaped ones, which are attributed to lack of fusion (LoF) effects (hereafter named "large pores"). Finally, cracks were isolated (Fig. 3c) and their area fraction was also estimated. The area fractions of small pores, of large pores, and of cracks corresponding to each parameter set within prints 1 and 2 are also included in Table 2. Finally, Fiji's directionality plug-in was also utilized to analyse the angular deviation (θ) of cracks with respect to BD (which is parallel to the vertical direction in the figure). In Fig. 3d the cracks have been coloured according to their θ angle following the colour coding included in the inset.

The (micro)structure of the printed samples was first characterized qualitatively by optical microscopy imaging of etched cross sections parallel to BD. The etching solution, consisting of 100 ml of 98% ethanol, 10 ml of 65% nitric acid, and 100 ml of distilled water [47], was applied to mirror-polished cross sections and it attacked preferentially the crystalline regions, allowing to detect their preferential location within melt pools. Etching was carried out by immersion during 15 s followed by water rinsing. XRD was also conducted on mirror-polished cross-sections parallel to BD to characterize qualitatively the presence of different phases (amorphous/crystalline) in the LPBF-manufactured parts. The amorphous fraction was additionally quantified by DSC using the same approach described above for powder characterization. Again, fully amorphous melt-spun ribbons were used as a benchmark [50]. The microstructure and microtexture of the crystalline regions of selected samples were evaluated by electron backscatter diffraction (EBSD) using an Apreo 2S (ThermoFisher Scientific) FEGSEM equipped with an Oxford Instruments EBSD detector, a CCD camera, and the Aztec data acquisition and analysis software package. Measurements were conducted at a working distance of 13 mm using an accelerating voltage of 20 kV, a beam current of 3.2 nA, and a step size of 80 nm. Grain sizes were estimated by separately averaging the length and width of 20 grains in different regions of EBSD inverse pole figure (IPF) maps.

Hysteresis loops at room temperature were measured with a Lake-Shore vibrating sample magnetometer (VSM) by applying a DC magnetic field in the range ± 1300 kA/m. The magnetic properties, such as the saturation mass magnetization (M_s) and the coercive field (H_c), were duly estimated from the hysteresis loops after appropriate subtraction of the diamagnetic signal from the sample holder.

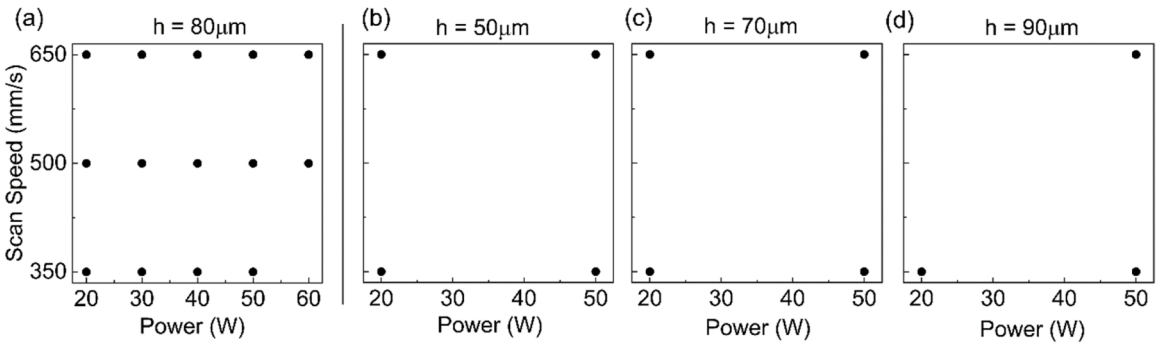

Fig. 2. Processing parameter combinations corresponding to (a) print 1 (KS1-KS14) and (b-d) print 2 (KS15-KS25).

Table 2
Relative density, area fraction of different defect types, and amorphous fraction of Kuamet6B2 additively manufactured samples.

Sample Name	Power (W)	Scan Speed (mm/s)	Hatch Distance (μm)	VED (J/mm^3)	Relative Density (%)	Small voids (%)	Large Voids (%)	Cracks (%)	Amorphous Fraction (%)
Print 1									
KS1	20	350	80	23	88.8	0.9	7.7	2.6	17
KS2	20	500	80	16	85.6	1.0	10.6	2.8	25
KS3	20	650	80	12	74.3	0.8	23.0	1.8	35
KS4	30	350	80	35	88.5	1.3	7.5	2.7	18
KS5	30	500	80	25	80.5	1.4	15.6	3.0	32
KS6	30	650	80	19	68.8	1.0	27.6	2.6	42
KS7	40	350	80	47	88.1	0.9	8.4	2.6	11
KS8	40	500	80	33	82.9	0.9	3.8	2.3	30
KS9	40	650	80	25	73.7	1.0	23.1	2.3	46
KS10	60	500	80	50	92.5	0.8	4.4	2.3	21
KS11	50	350	80	59	93.1	0.7	3.5	2.7	20
KS12	50	500	80	41	90.0	0.9	6.5	2.6	25
KS13	50	650	80	32	85.8	0.9	10.8	2.4	21
KS14	60	650	80	38	81.1	1.0	15.4	2.4	34
Print 2									
KS15	20	350	50	38	90.8	0.6	6.5	2.1	10
KS16	20	350	70	27	91.1	0.7	5.8	2.4	14
KS17	20	350	90	21	89.4	0.9	7.4	2.2	24
KS18	20	650	50	26	85.2	0.8	12.1	2.0	27
KS19	20	650	70	19	75.2	0.7	22.2	1.8	36
KS20	50	350	50	95	91.8	0.6	5.4	2.2	3
KS21	50	350	70	68	92.0	0.6	5.1	2.3	11
KS22	50	350	90	53	92.9	0.7	4.0	2.4	18
KS23	50	650	50	67	87.1	0.8	9.9	2.2	24
KS24	50	650	70	48	81.4	1.0	15.7	2.0	36
KS25	50	650	90	37	76.6	1.0	20.6	1.7	42

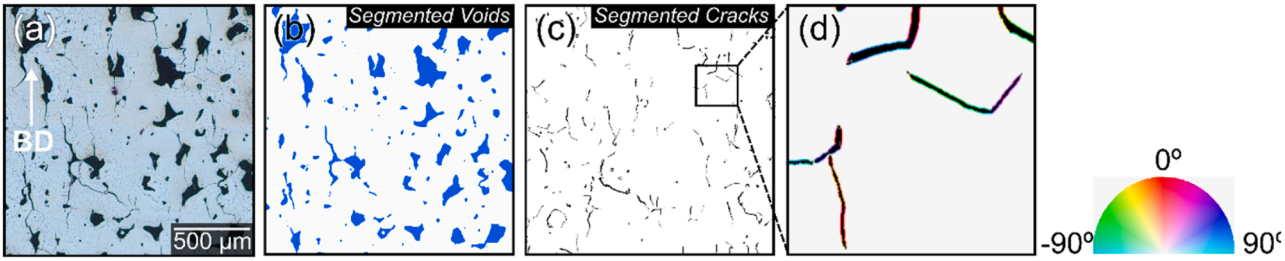

Fig. 3. Schematic illustrating the workflow of the machine-learning based image segmentation procedure utilized for defect characterization. (a) Optical micrograph illustrating, in black, the defect structure; (b) binarized image of voids (including small and large pores), shown in blue; (c) binarized image of cracks; (d) colour coding for the angular deviation of cracks with respect to the BD (0°).

3. Results

3.1. Effect of LPBF processing parameters on the defect structure

Fig. 4 illustrates the defect structure along a cross-section parallel to BD in all samples manufactured within prints 1 (KS1-KS14) and 2 (KS15-KS25). The corresponding density values, along with the area fraction of small pores, large pores, and cracks, are included in Table 2. The area fraction of small voids generated by trapped gas or by keyhole effects is small (around 1%) irrespective of the processing parameters. Conversely, the area fraction of large voids, originated by lack of fusion of the feedstock powder, ranges from 3.5 to 27.6% and it depends strongly on the processing conditions. Finally, the area fraction of cracks ranges from 1.7% to 3.0% within the processing window investigated in the present study. Fig. 5 is a colour map illustrating the variation of the density of the LPBF manufactured parts with respect to the processing parameters for samples manufactured within prints 1 (Fig. 5a) and 2 (Figs. 5b-d). The actual measurements have been plotted using solid black dots and colour coding has been utilized to build the map by interpolation of the measured data. It can be seen that, for a fixed value of the hatch distance, the density increases when using processing conditions that combine high power and low scan speed. The difference between the maximum and minimum density values obtained for each hatch distance ($\Delta\rho_h$) increases with increasing hatch distance. Overall, the highest density (93.1%) was achieved in sample KS11 (50 W, 350 mm/s, h = 80μm) and the lowest (68.8%) was detected in sample KS6 (30 W, 650 mm/s, h = 80μm).

Fig. 6 illustrates the orientation of the cracks in sample KS1, measured using the image analysis tool described in Fig. 3d. The angle θ represents the inclination of each crack with respect to BD. Cracks lie preferentially at θ angles that are symmetric with respect to the build direction. In particular, higher frequencies of cracks appear at θ values of approximately 0°, ±5°, ±15°, ±20°, ±25°, ±45°, ±50°, ±70°, and 90°. Comparatively, the frequency of cracks at said orientations is slightly higher for the negative θ values than in their positive counterpart with the exceptions of ±5° and ±20°, where the frequency is roughly the same on both sides of the histogram. Examination of the crack orientation in all processed samples yielded identical results.

3.2. Effect of LPBF processing parameters on crystallization

Irrespective of the processing conditions, a two-phase (amorphous/crystalline) structure was obtained following LPBF processing of the Kuamet6B2 alloy under investigation. Fig. 7 compares the XRD patterns corresponding to all the samples processed using the conditions included in prints 1 and 2 with that of a reference fully amorphous Kuamet6B2

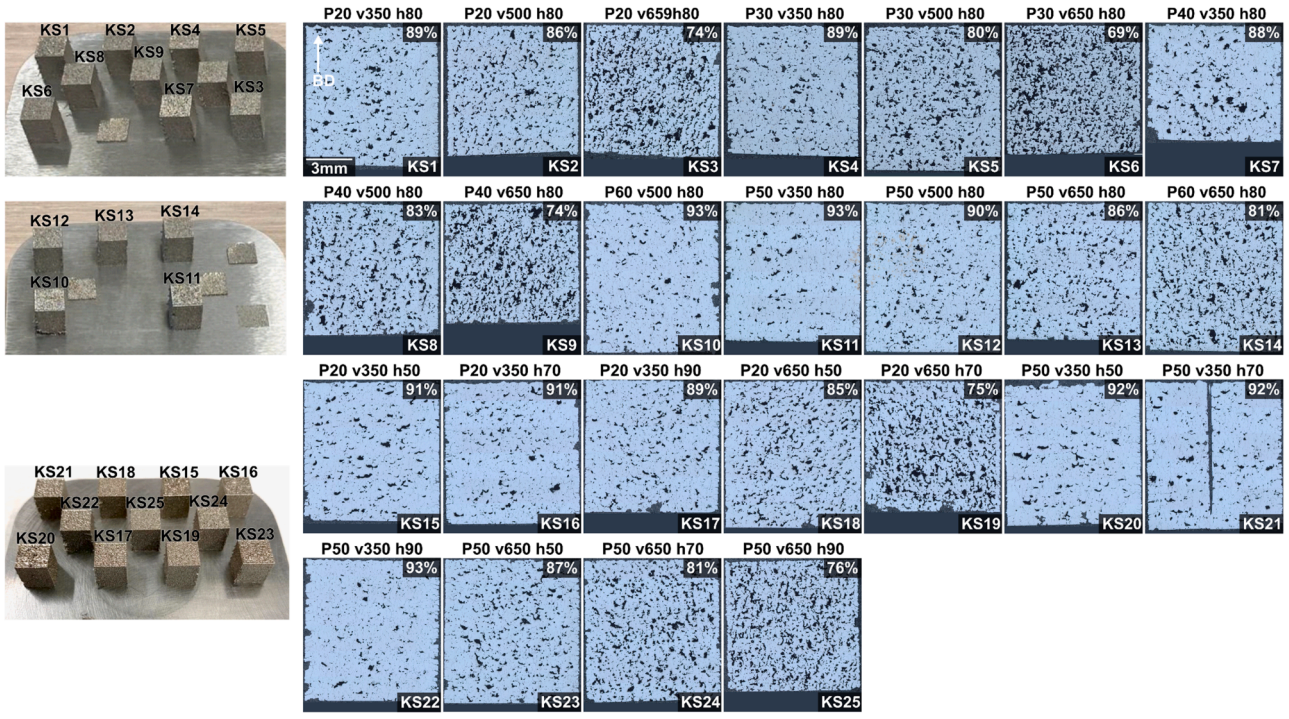

Fig. 4. As-built prisms manufactured within print 1 (KS1-KS14) and print 2 (KS15-KS25) as well as the corresponding optical micrographs illustrating the defect structure along a cross-section parallel to the BD. The density values estimated by image analysis have been included as insets on the top right corner of each image.

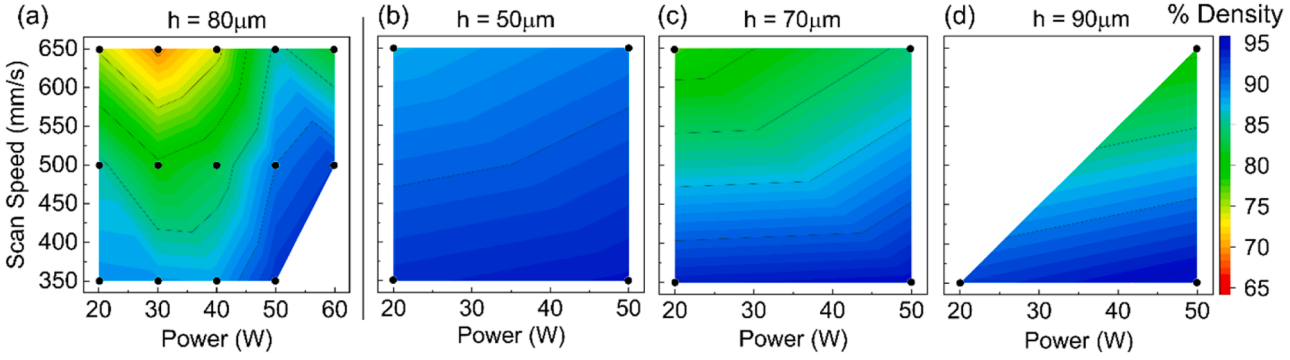

Fig. 5. Colour maps illustrating the variation of the density of the LPBF manufactured parts as a function of the processing parameters. (a) Print 1; (b) print 2, $h = 50$ μm; (c) print 2, $h = 70$ μm; (d) print 2, $h = 90$ μm. The solid black dots indicate the actual measurements. The maps have been constructed by interpolation.

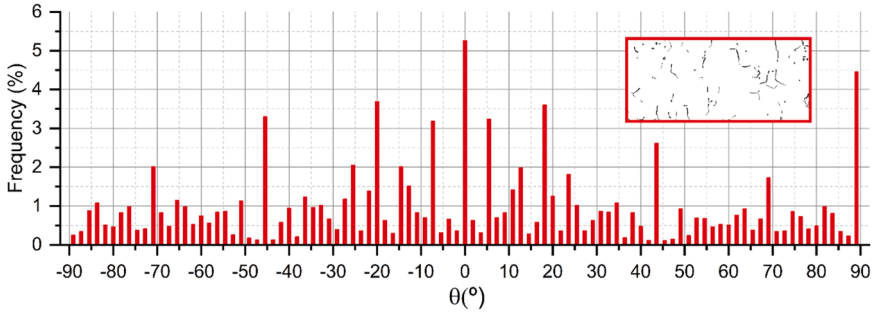

Fig. 6. Histogram representing the orientation of cracks with respect to the BD on sample KS1.

melt-spun ribbon and with that of spinning water atomized powders with the same alloy composition. The ribbon exhibits an amorphous hump at diffraction angles comprised between 40° and 50°, in the absence of any distinct diffraction peaks. The powder pattern is formed by the superposition of a very similar hump with a small intensity peak at 45°. The latter might be attributed to either α-Fe or Fe_3Si, as these two phases cannot be unambiguously distinguished by XRD [58]. The XRD patterns from all printed samples, however, show a slight amorphous

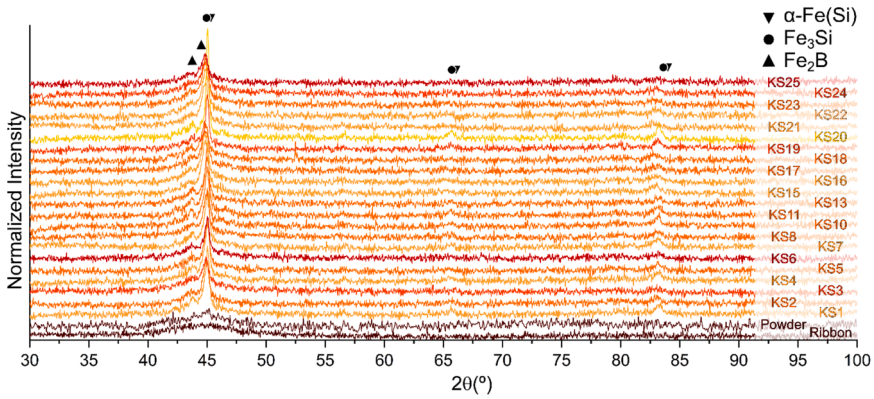

Fig. 7. Comparison of the XRD patterns corresponding to the Kuamet6B2 samples fabricated using the parameter sets included in prints 1 (KS1–KS14) and 2 (KS15–KS25) with those of reference melt-spun ribbons and of gas atomized powder with the same alloy composition.

hump located at the same diffraction angle as the ribbons and the powder, as well as pronounced superimposed peaks, which may be attributed to the presence of the α-Fe/Fe_3Si and Fe_2B phases, which are known to be formed during the solidification of Fe-Si-B BMGs [58,59]. The presence of an amorphous/crystalline composite-like structure following LPBF of this alloy is consistent with earlier reports [47]. XRD did not reveal the presence of oxides.

The spatial distribution of the amorphous and crystalline phases is, qualitatively, similar for all LPBF parameter combinations investigated (KS1-KS25). As an example, Fig. 8 provides a qualitative view of the amorphous and crystalline regions in an etched cross-section parallel to the BD in sample KS7. The amorphous phase appears with light contrast, while areas populated by crystallites appear as brown regions, as they are selectively corroded during etching. The top layer in Fig. 8 is populated by melt pools containing a much larger fraction of amorphous phase than those present at the interior of the printed sample. This confirms that crystallization does not take place preferentially during solidification but that it occurs on the HAZ as a consequence of the overlap between neighbouring tracks or between consecutive layers. Indeed, it can be clearly seen in Fig. 8 that crystalline regions are predominantly located both at the left-hand side of melt pools (HAZ of neighbouring tracks) and at the bottom of melt pools (HAZ of subsequent layers). The thickness of the corroded regions, i.e., the degree of crystallization, was found to be highly dependant on the parameter combination used. Further quantification of crystallization is provided below.

Fig. 9 includes several colour maps illustrating the variation of the fraction of the amorphous phase, measured by DSC (Supplementary Fig. 1), as a function of the processing parameters for samples processed within prints 1 (Fig. 9a) and 2 (Figs. 9b-d). The actual measurements have been plotted using solid black dots and colour coding has been utilized to build the map by interpolation of the measured data. The amorphous fraction values corresponding to each processing condition investigated are listed in Table 2. For a fixed value of the hatch distance, the fraction of the amorphous phase increases when using processing conditions that combine low power and high scan speed. In particular, the largest value (46%) was measured on sample KS9 (40 W, 650 mm/s, $h = 80$ μm) and the lowest value (3%) was found on sample KS20 (50 W, 350 mm/s, $h = 50$ μm). The difference between the maximum and the minimum fractions of amorphous phase obtained for each hatch distance increases as h increases from 50 to 90 μm. Comparison of Figs. 9 and 5 reveals that amorphous fraction decreases when LPBF is carried out under conditions for which the density increases. Such inverse relationship between amorphous fraction and the relative density, which also applies to other BMGs processed by LPBF [16,18], represents a critical challenge for LPBF process optimization of Kuamet6B2.

In Fig. 10 the amorphous fraction values are related to the processing parameters (v,P,h) for all samples manufactured within prints 1 (KS1-KS14) and 2 (KS15-KS25). The results are grouped by hatch distance (black dashed rectangles with rounded corners). Yellow, orange, and red squares correspond, respectively, to $v = 350$ mm/s, 500 mm/s, and 650 mm/s. Fig. 10 reveals that, irrespective of h, for a given v, changing P from 20 to 50–60 W has a relatively small influence on amorphous fraction whereas for a fixed P, increasing v from 350 to 650 mm/s leads to a significant increase in amorphous fraction. As explained in Section 2, v was modified by altering the laser exposure time while keeping the point distance constant. Thus, the data of Fig. 10 reveal that altering the exposure time of the pulsed laser has a stronger influence on amorphous fraction than changing P.

The microstructure and the microtexture within crystalline regions were examined by SEM and EBSD and were found to be similar for all processing conditions. As an example, Fig. 11 illustrates the microstructure of two samples processed with very different parameters: KS19, with $P = 20$ W, $v = 650$ mm/s, and VED=10 J/mm^3 (Figs. 11a-c) and KS20, with $P = 50$ W, $v = 350$ mm/s, and VED=95 J/mm^3 (Figs. 11d-f). Figs. 11a and 11d are SEM micrographs obtained in the SE mode in which several cracks traversing melt pools can be appreciated. Figs. 11b and 11e are EBSD phase maps in which α-Fe/Fe_3Si crystallites are coloured in red, $Fe_{23}B_6$ grains are coloured in blue, and Fe_2B crystals are coloured in green, while darks areas are zero-solutions, associated to amorphous or nano-crystalline regions with sizes below the instrument's resolution. Finally, Figs. 11c and 11f are EBSD IPF maps in the BD in which grains are coloured following the colour coding included as an inset. Figs. 11c and 11f also contain the corresponding inverse pole figures illustrating the orientation of the BD. Fig. 11 confirmed, first, that crystalline regions are preferentially located at the perimeter of melt pools, as was inferred from the etched optical micrograph of Fig. 8. Second, the EBSD phase maps of Figs. 11b and 11d reveal that the largest fraction of crystallites corresponds to the α-Fe/Fe_3Si phases (coloured in

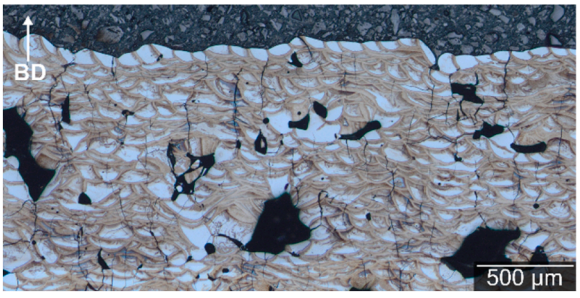

Fig. 8. Optical image of an etched cross-section parallel to the BD in sample KS7. The amorphous phase appears with light contrast, while areas populated by crystallites appear as darker regions, as they are selectively corroded during etching. In the top layer the tracks are perpendicular to the imaged cross-section.

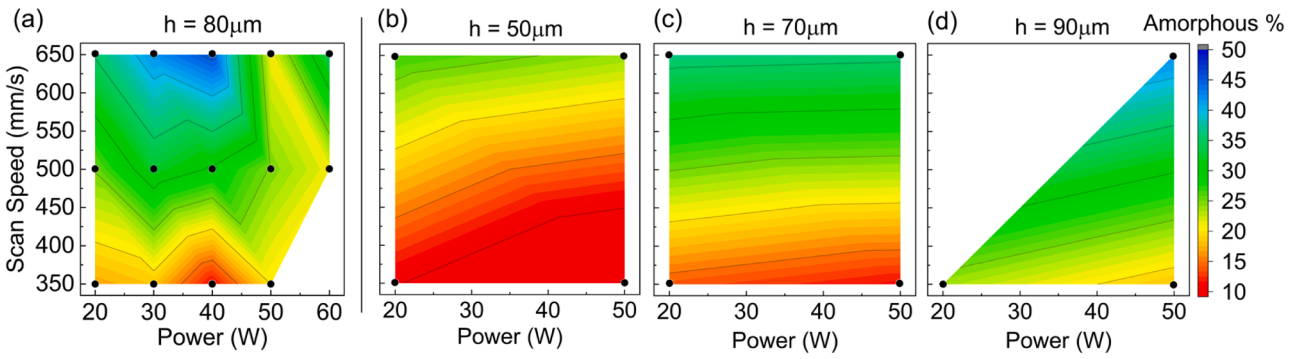

Fig. 9. Colour maps illustrating the variation of the amorphous fraction, measured by DSC, in the LPBF-manufactured samples as a function of the processing parameters. (a) Print 1; (b) print 2, $h = 50$ μm; (c) print 2, $h = 70$ μm; d) print 2, $h = 90$ μm.

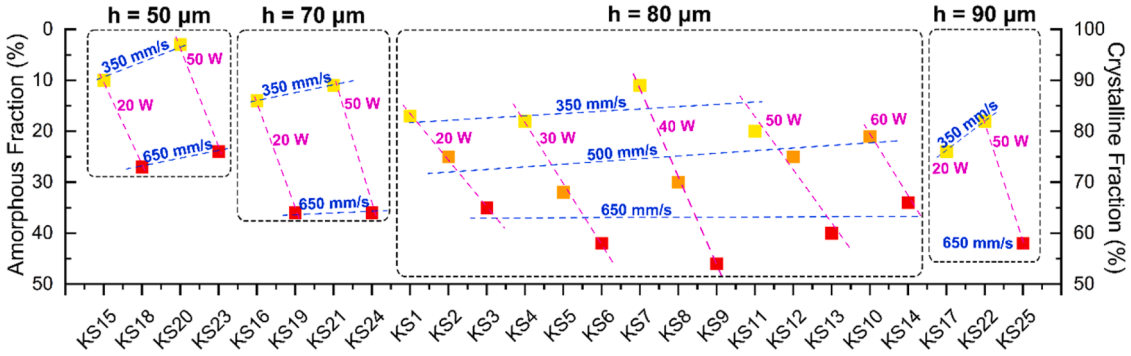

Fig. 10. Amorphous fraction of all samples processed within prints 1 (KS1–KS14) and 2 (KS15–KS25) as a function of the LPBF processing parameters. The results are grouped by h (black dashed rectangles with rounded corners). Yellow, orange, and red squares correspond, respectively, to $v = 350$ mm/s, 500 mm/s, and 650 mm/s.

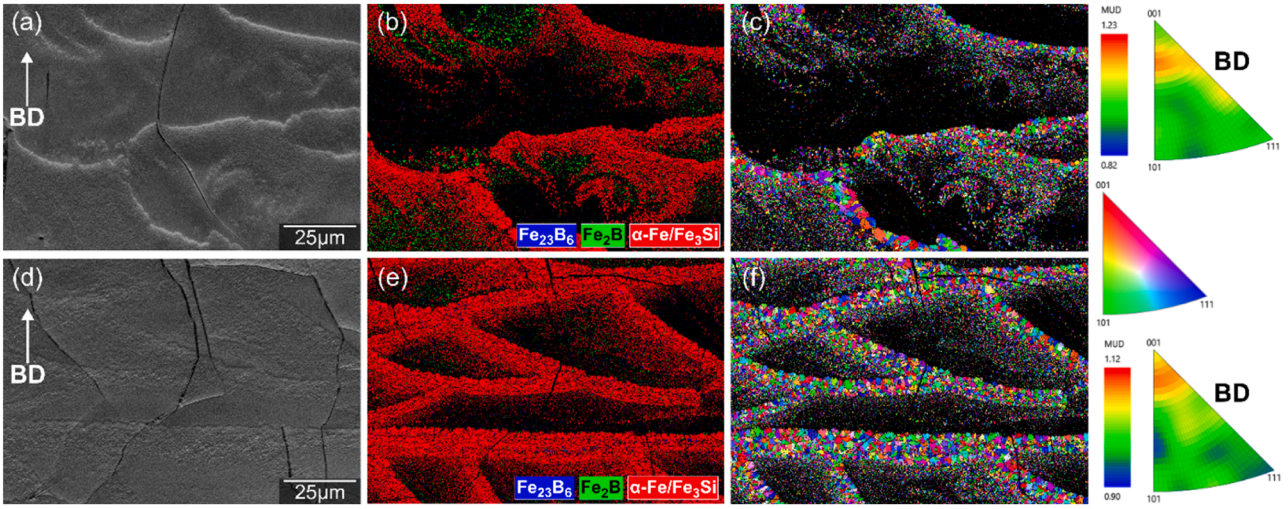

Fig. 11. Microstructure and microtexture within crystalline regions in LPBF processed Kuamet6B2 KS19 (a-c) and KS20 (d-f) samples. a, d) Secondary electron SEM images; b, e) EBSD phase maps; c, f) EBSD IPF maps in the BD and the corresponding inverse pole figures illustrating the direction of BD.

red), which cant be distinguished unambiguously by this technique due to the similarity between the crystalline lattice parameters of the two phases [10,58]. Third, the fraction of borides (coloured in blue and green) seems to be higher in the sample processed with a lower energy density (KS19) (Fig. 11b). Fourth, crystalline regions are formed by randomly orientated, mostly equiaxed grains, with sizes under 4 μm (Figs. 11c and f). The largest grains are found at the bottom of melt-pools, while ultrafine and nanocrystalline grains with sizes under 1 μm tend to be dispersed within amorphous regions at the melt-pool cores.

3.3. Magnetic properties

Room temperature hysteresis loops of all printed samples, of the feedstock powder and of the melt-spun ribbon were measured. A representative selection of *M(H)* curves is shown in Fig. 12. The ribbon shows the typical *M(H)* curve of a soft magnetic material characterized by a fully amorphous microstructure, i.e., a regime of full saturation achieved at a low magnetic field that reverses in a narrow magnetic field range. As a result, a high magnetic susceptibility (the slope of M curve with increasing H) and a very low coercive field (lower than the

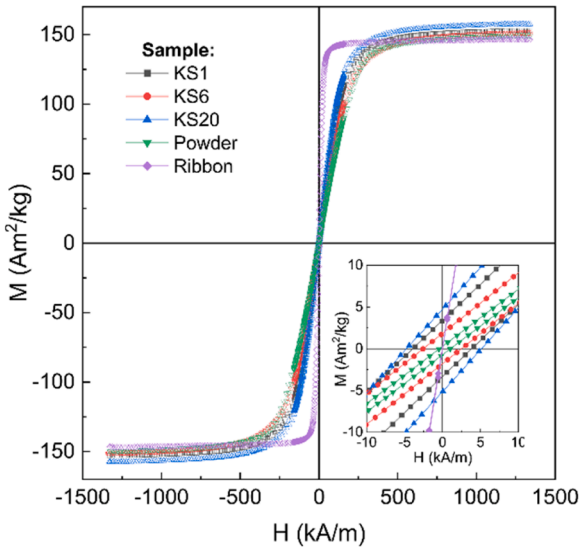

Fig. 12. Room-temperature hysteresis loops of selected printed samples, of the feedstock powder, and of melt-spun ribbon. An enlarged view of the of M(H) curves at low magnetic field is shown as an inset.

sensitivity of VSM, as shown in the inset) are measured. Conversely, the magnetization reversal process of the *M(H)* curves for the printed samples and for the powder takes place over a wider magnetic field interval with a reduce magnetic susceptibility. These characteristics are compatible with the reduction of the amorphous fraction observed in these samples compared to the as-quenched ribbon. The crystalline phase would hinder the movement of the domain walls affecting both the magnetic field strength needed to reach saturation as well as the values of saturation magnetization and coercivity (the latter is now detectable by VSM, as shown in the inset). Finally, while the magnetization process measured in the powder displays almost the same susceptibility value as the printed samples, the coercivity is lower due to the presence of a higher fraction of the amorphous phase.

Fig. 13a depicts the saturation mass magnetization, M_s, of the samples manufactured within prints 1 and 2 (blue squares) as a function of the amorphous fraction (estimated by DSC measurements). The M_s values corresponding to the feedstock powder (149 Am^2/kg, yellow triangle) and to a fully amorphous ribbon (147 Am^2/kg, red circle) are included in the plot for reference. M_s decreases slightly as the amorphous fraction increases. As the Fe content is the same in all samples independently on the synthesis process, the M_s, which is an intrinsic property of the alloy, is expected to be the same in all measured samples. The reduction of M_s with increasing amorphous fraction observed in Fig. 13a is ascribed to a lower magnetic moment of the amorphous Fe-based alloy phases with respect to that of the Fe-based crystalline phases [60].

Fig. 13b shows the coercive field (H_c) of all samples processed within prints 1 and 2 as a function of the corresponding amorphous fraction (estimated by DSC measurements). The values corresponding to the feedstock powder (amorphous fraction of 82%) and to a fully amorphous ribbon are included in the plot for reference. It is evident that, overall, the coercivity decreases as amorphous fraction increases. Indeed, the lowest coercive field (H_c=2.5 kA/m) was measured on sample KS6, with one of the highest amorphous fractions (42%), while the highest coercive field (H_c=5.0 kA/m) was measured on sample KS21, in which the amorphous fraction is rather low (11%). Irrespective of the printing conditions, H_c in the LPBF-processed samples is three orders of magnitude higher than in the amorphous ribbon, which confirms that crystallization severely hinders the soft magnetic response. Microstructural parameters such as the average grain size do not appear to have a significant influence on H_c.

In Fig. 14 the H_c values are related to the processing parameters (v,P, h) for all samples manufactured within prints 1 (KS1-KS14) and 2 (KS15-KS25). The results are grouped by hatch distance (black dashed rectangles). Yellow, orange, and red squares correspond, respectively, to v = 350 mm/s, 500 mm/s, and 650 mm/s. The H_c value of a fully amorphous melt-spun ribbon (6.2 A/m) has been added as a reference. It is apparent that, for a given v, changing P from 20 to 50–60 W has a minor influence on H_c, whereas for a fixed P, increasing v from 350 to 650 mm/s leads to a significant reduction of H_c. Moreover, when h is increased from 50 to 90 μm, the said impact of the scanning speed on H_c is further accentuated. As explained in Section 2, v was modified by altering the laser exposure time while keeping the point distance constant. Thus, the data of Fig. 14 reveal that altering the exposure time of the pulsed laser has a stronger influence on H_c than changing P (within the ranges investigated). Comparison of Fig. 14 with Fig. 10 confirms that the strong effect of v on H_c can be directly related to the similarly strong effect of v on the amorphous fraction.

4. Discussion

4.1. Analysis of crack propagation

Optimization of LPBF of Fe-based BMGs for soft-magnetic

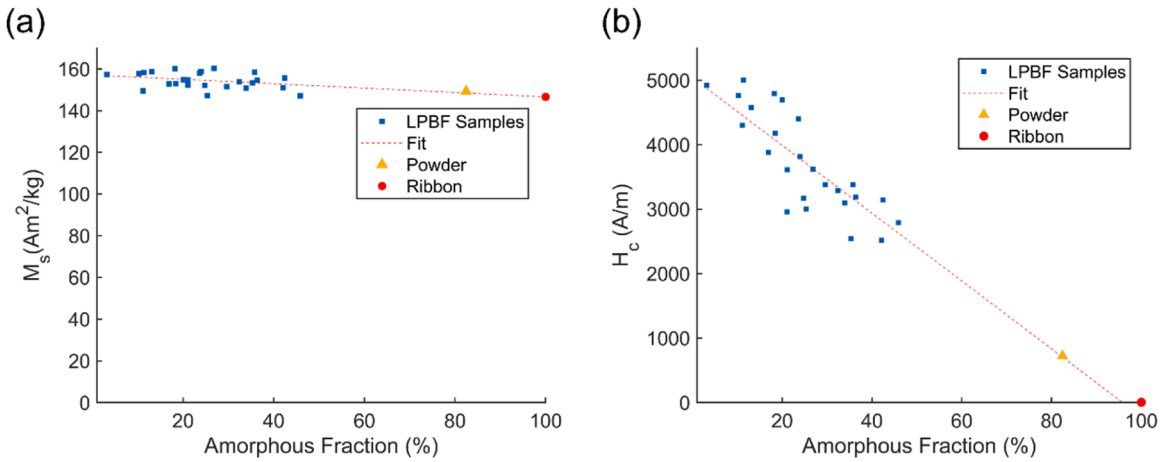

Fig. 13. (a) Saturation mass magnetization (M_s) and (b) coercive field (H_c) as a function of the amorphous fraction. Blue squares represent the LPBF manufactured samples (prints 1 and 2). The values corresponding to the feedstock powder (yellow triangle) and melt-spun, fully amorphous, ribbon (red circle) of the same composition are included as a reference.

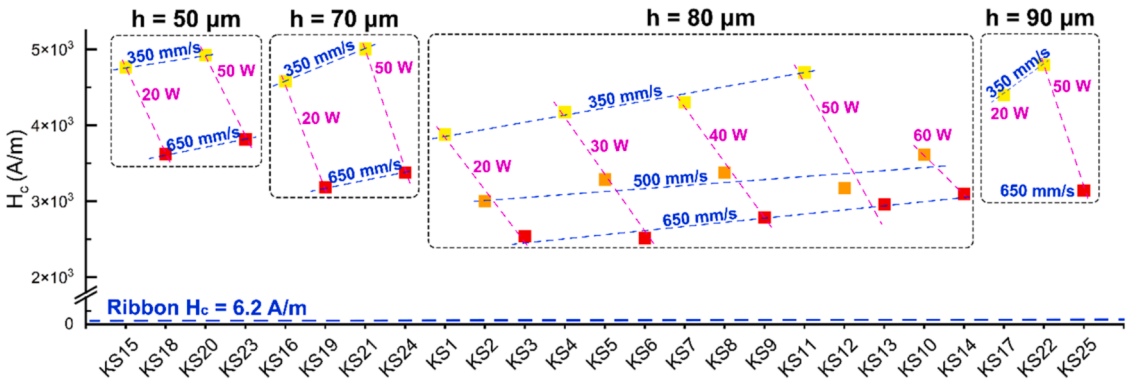

Fig. 14. Coercive field (H_c) of all samples processed within prints 1 (KS1–KS14) and 2 (KS15–KS25) as a function of the LPBF processing parameters. The results are grouped by hatch distance (black dashed rectangles). Yellow, orange, and red squares correspond, respectively, to v = 350 mm/s, 500 mm/s, and 650 mm/s. The value corresponding to a fully amorphous melt-spun ribbon is presented as reference.

applications requires a thorough understanding of crack nucleation and propagation mechanisms. Earlier works on LPBF of Fe-based BMGs have reported that crack nucleation takes place preferentially at pores [33], as they act as stress concentration points, or at the junction of crystalline and amorphous regions [36,38] owing to the local stresses generated by the different volume shrinkage of the two phases during solidification. Comparatively less work has been carried out on the analysis of crack propagation paths.

Our research shows that cracking is present in all the LPBF-processed Kuamet6B2 samples, irrespective of the processing conditions, and that the area fraction occupied by cracks remains always between 1.8 and 3% (Table 2). Fig. 6 shows that cracks propagate preferentially at θ values of approximately 0°, ±5°, ±15°, ±20°, ±25°, ±45°, ±50°, ±70°, and 90° with respect to BD. In Fig. 15 we relate the orientation of crack propagation paths to the morphology of the crystalline regions. The latter is "quantified" by measuring the orientation of the directions perpendicular to the facets of crystalline/amorphous interfaces (normal directions, NDs) as described in Figs. 15 (a-d). In particular, the distribution of inclination angles of all the NDs with respect to BD (θ) was analysed by segmenting optical micrographs of etched surfaces (Fig. 15a) into amorphous (Fig. 15b) and crystalline (Fig. 15c) as described in Section 2. In Fig. 15d the facets along the crystalline/amorphous interfaces have been coloured according to their θ' angle following the colour coding included in the inset. Fig. 15e compares the θ (red bars, data from Fig. 6) and θ' (blue bars) distributions in sample KS1. Both distributions are remarkably similar, with almost overlapping high frequency peaks, thereby confirming that cracks propagate preferentially along directions that are perpendicular to the crystalline/amorphous interfaces. Moreover, the amorphous/crystalline interfaces show higher frequencies at positive angles than their negative counterparts, which is the opposite that was observed for the crack orientations, further confirming that cracks preferentially grow perpendicular to the crystalline/amorphous interfaces. The difference in frequency observed on both sides of the histograms can be explained by the overlap of adjacent tracks, which generate crystalline HAZ's that are asymmetric about the BD (Figs. 8 and 11). This phenomenon was observed on several Kuamet6B2 samples processed using widely different sets of LPBF processing parameters (KS1, KS15-KS25). These results suggest that crack propagation is mainly dependant on the melt pool geometry and on the degree of periodic overlap of crystalline regions following LPBF processing [36,38,44].

Goodall et al. [55] have recently reported how altering crack propagation paths in a Fe-Si steel processed by LPBF can be a very useful tool to increase the resistance in the planes in which eddy currents circulate, thereby reducing energy losses. They succeeded to control crack density and crack propagation paths by tuning the LPBF processing parameters

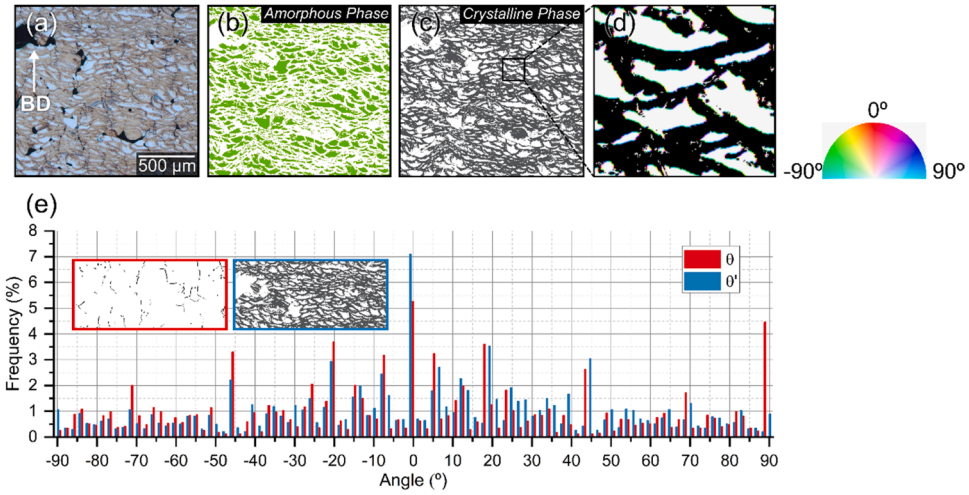

Fig. 15. Schematic of the workflow followed to analyse the paths of preferential crack propagation by image analysis. (a) Etched optical micrograph illustrating, in brown contrast, crystalline regions and in light contrast, amorphous regions; (b,c) binarized images highlighting amorphous (green, b) and crystalline (grey, c) phases; (d) enlarged view of a region of (c) in which facets along the crystalline/amorphous interfaces have been coloured according to the orientation of their normal direction following the colour coding included in the inset. (e) Histogram comparing the preferential orientations of cracks (red bars, θ) and of the directions perpendicular to the different facets along the crystalline/amorphous interphases (blue bars, θ) in the LPBF manufactured Kuamet6B2 KS1 sample.

and the scanning strategy. Our data suggest that controlling melt pool shapes and sizes, and thus the corresponding HAZ, may constitute a useful tool to design crack propagation paths in LPBF-manufactured Fe-based BMGs.

4.2. Scan strategy as a tool to achieve high density levels and high amorphous fraction simultaneously

The present work has shown the effect of some of the main LPBF processing parameters on the fraction of internal defects, on the generated (micro)structure and on the corresponding magnetic properties. For instance, high P, low v, and low h combinations give rise to high relative density and highly crystalline samples, endowed with high M_s and high H_c. On the other hand, parameter sets including low P, high v, and high h lead to samples with lower relative density and with higher amorphous fraction, which thus possess slightly smaller M_s and a significantly lower H_c. Such findings are coherent with the few works published in the literature on LPBF of similar Fe-based BMGs [21,28,48-50]. It therefore becomes clear that when using a simple scanning strategy, such as the one adopted in the current study (meander), there are no combinations of P, v, and h that will allow to manufacture samples with both the density *and* the M_s and H_c values required for soft magnetic applications.

Several approaches to overcome the barriers to manufacture Kuamet BMG alloys with high densities *and* large amorphous fraction by LPBF have been reported recently [48-50]. Table 3 compares the values of density, amorphous fraction, M_s and H_c corresponding to these studies with those of the current work. The most successful approach, involving the use of a two-pass scanning strategy, was reported by Zrodowski et al. [48] in 2019. The first pass, in which the laser followed a chessboard strategy, would melt the powder once. During the second pass, without depositing a new powder layer, the laser was programmed to follow a "point-random strategy", which consisted on melting single points separate from each other in a random fashion, until the full surface had been re-melted. This strategy yielded, simultaneously, an amorphous fraction of 90% and a maximum relative density of 94%. The material used in this study was Kuamet 52, which has a slightly different composition ($Fe_{71}Si_{10}B_{11}C_6Cr_2$ [at.%]) from that of the Kuamet6B2 used for the presented work. The drawbacks of this complex scanning strategy are a considerable increase in build time and the difficulty to replicate it with commercial LPBF systems. In 2020 Nam et al. [49] proposed a double scanning strategy to manufacture Kuamet6B2 by LPBF where the laser would first melt a powder layer following a meander path and, without depositing a new layer, it would then re-melt the solid material following a second meander path rotated 90° with respect to the previous scan. This yielded an amorphous fraction up to 47% in samples with a density of 96%. Although this double-pass approach is simpler than the point-random strategy, the main drawback continues to be the considerable increase in production time. In 2022 Thorsson et al. [50] manufactured by LPBF a record-large Kuamet6B2 rotor prototype with an amorphous fraction of 70% and with a density of approximately 98% using an advanced scanning strategy that was not disclosed. Further efforts are required to devise advanced scanning strategies that allow to overcome the "density/amorphous fraction" paradox without significantly compromising productivity.

4.3. Origin of the strong effect of the scanning speed on crystallization

A key finding of the present study is that, for a given hatch distance, v and, more specifically, the laser exposure time, has a significant effect on crystallization, and thus on H_c, than P (Figs. 10 and 14), at least when these parameters are changed within the ranges investigated. Since the investigated Fe-based BMG is targeted for soft magnetic applications, for which achieving very low H_c values is of paramount importance, understanding the origin of the dominant effect of v is key to devise guidelines for LPBF process optimization.

On the other hand, our results also show (Fig. 8) that crystallization takes place preferentially because of the heating resulting from the deposition of neighbouring tracks and of consecutive layers. For fixed hatch and layer thickness values, the overall volume of the HAZ will, in general, increase with the melt pool size [12], as larger melt pools give rise to a higher degree of overlap between neighbouring tracks and between consecutive layers, respectively. In the following, the effect of v and P on the melt pool dimensions is analysed. Fig. 16 illustrates the evolution of the average melt pool's width (w) and depth (d) with v (Figs. 16a,c) and with P (Figs. 16b,d) in samples manufactured within print 1 ($h = 80$ μm). Several observations can be made from this figure. First, the fact that $d/w < 1$ for all conditions investigated, together with the semi-circular shape of the melt pools (Fig. 8), evidences that LPBF processing was carried out within the conduction mode [10,54,61-66]. Second, w decreases with increasing v (Fig. 16a) but remains invariant with changes in P (Fig. 16b). Third, d is basically independent of v (Fig. 16c) and of P (Fig. 16d). Altogether, these data suggest that the average melt pool's cross-section and, thus, the HAZ, decreases with increasing v, while remaining almost invariant with P.

In Fig. 17 the melt pool's widths of samples KS1-KS25 are related to the corresponding processing parameters (v,P,h). The results are grouped by hatch distance (black dashed rectangles). Yellow, orange, and red squares correspond, respectively, to $v = 350$ mm/s, 500 mm/s, and 650 mm/s. It is apparent that v has a more significant influence than P on the melt pool's width, at least within the parameter range investigated in the present study. Moreover, when h is increased from 50 to 80 μm, the said impact of v on the melt pool's width is further accentuated. Comparison of Fig. 17 with Figs. 10 and 14 suggests that the origin of the dominant effect of v on amorphous fraction (and therefore on H_c) is, at least partially, related to the stronger influence of v than of P on the melt pool size (and, thus, on the corresponding HAZ). Therefore, optimizing v (by tuning the exposure time) might constitute a valuable tool for the design of LPBF-manufactured Fe-based metallic glasses with reduced H_c and high M_s and thus to improve the soft magnetic behaviour.

Although it is widely agreed that the melt pool size and, in particular, the melt pool width, increase with the VED [67-71], further efforts are needed to understand the effect of isolated processing parameters such as v and P on melt pool geometry for each metallic alloy class [64,68,69,72-74]. In the present work the prevalent influence of v on w described above is not related to the overall VED level as, for example, within print 1, at $P = 30$ W, increasing v between 350 and 650 mm/s leads to a decrease of VED between 35 and 19 J/mm^3 (Table 2, $\Delta_{VED}=-16\ J/mm^3$) and to a decrease of the melt pool width of 20 μm while, at $v = 500$ mm/s, increasing P between 20 and 60 W leads to an increase of VED between 16 and 41 J/mm^3 (Table 2, $\Delta_{VED}=25\ J/mm^3$) and to an

Table 3
Comparison of the relative density, amorphous fraction, and magnetic properties achieved in this study with those reported in the literature for similar alloys [48-50].

Reference	Material [at.%]	Sample Geometry	Density (%)	Amorphous Fraction (%)	M_s (T)	H_c (A/m)
Zrodowski 2019 [48]	$Fe_{71}Si_{10}B_{11}C_6Cr_2$	Discs (∅5 mm x 1 mm)	94	90	1.30	397
Nam 2019 [49]	$Fe_{73.7}B_{11}Si_{11}Cr_{2.3}C_2$	Prisms (10 × 10 × 5 mm^3)	96	47	1.22	1600
Thorsson 2022 [50]	$Fe_{73}Si_{11}B_{11}C_3Cr_2$	Rotor (∅60 mm x 46 mm)	98	70	1.29	510
This work KS11	$Fe_{73.7}B_{11}Si_{11}Cr_{2.3}C_2$	Prisms (8 × 8 × 9.5 mm^3)	93	20	**1.23***	**4697**
This work KS9	$Fe_{73.7}B_{11}Si_{11}Cr_{2.3}C_2$	Prisms (8 × 8 × 9.5 mm^3)	74	46	**1.19***	**2790**

* Note that the saturation values in printed samples (KS9 and KS11) have been calculated by using the nominal density of the Kuamet6B2 alloy.

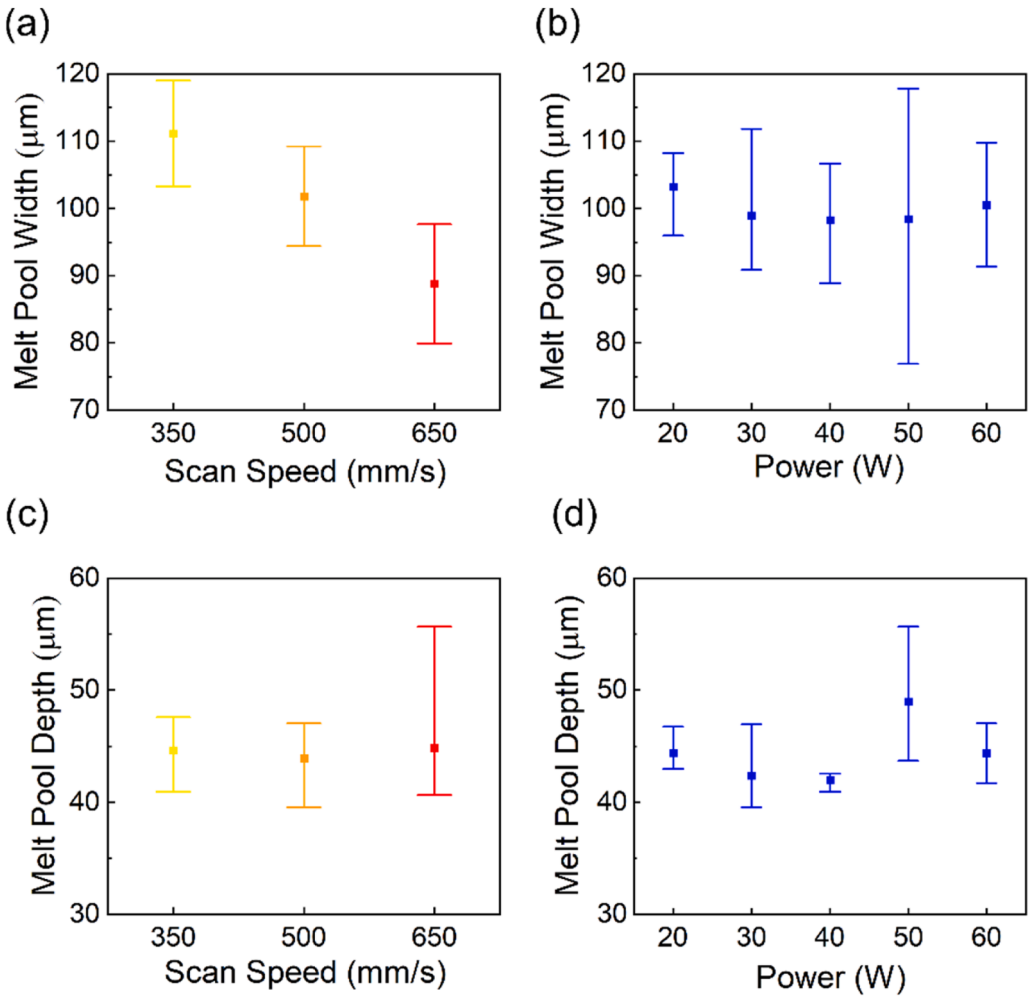

Fig. 16. (a) Average melt pool width with respect to v; (b) average melt pool width with respect to P; (c) average melt pool depth with respect to v; (d) average melt pool depth with respect to P. The error bars represent the minimum and maximum averages amongst the samples of each parameter group.

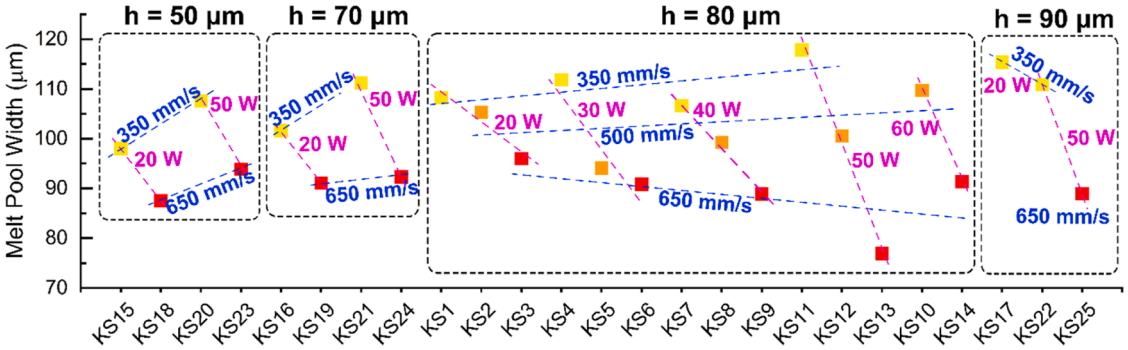

Fig. 17. Melt pool widths of all samples processed within prints 1 (KS1–KS15) and 2 (KS15–KS25) as a function of the LPBF processing parameters. The results are grouped by hatch distance (black dashed rectangles). Yellow, orange, and red squares correspond, respectively, to v = 350 mm/s, 500 mm/s, and 650 mm/s.

increment of the melt pool size of only 4 µm. That is, within a similar VED range, comparable changes in VED achieved by changing either v or P led to larger variations of the melt pool geometry when altering v. This research, thus, suggests, that, within the LPBF parameter ranges investigated, changes in v (by altering the exposure time) have a stronger effect in heat conduction than altering P.

4. Conclusions

This study aims to establish a relationship between the LPBF processing parameters, the (micro)structure, and the magnetic behaviour of a Fe-based Kuamet6B2 BMG for soft magnetic applications. With that purpose, an extensive range of LPBF process parameter sets (P, v, and h), a simple meander strategy, and a fixed layer thickness of 30 µm, were utilized to manufacture simple geometry specimens. The LPBF processing parameters were related to (micro)structural features such as the

density, the area fraction of pores and cracks, the fraction of amorphous and crystalline phases, and the microstructure of the crystalline regions. Finally, soft magnetic properties such as M_s and H_c were measured and related to the LPBF parameters and to the (micro)structure. The following conclusions can be drawn from the present work.

1. Within the entire LPBF processability window the manufactured samples present composite-like structures formed by crystalline and amorphous phases. Crystallization occurs preferentially in the HAZs surrounding melt pools due to the melting of neighbouring layers or of consecutive passes. Crystalline regions are formed by α-Fe/Fe_3Si, $Fe_{23}B_6$, and Fe_2B equiaxed grains with random orientations and sizes ranging from a few microns to the nano regime.
2. In the conduction regime investigated here, the parameter sets giving rise to the highest densities (high P, low v) caused the most crystallization and, in turn, settings leading to high porosity (low P, high v) allowed the material to retain the highest amorphous fraction after fabrication. In particular, the highest density (93.1%) was achieved in a sample that was 20% amorphous, while the highest amorphous fraction (46%) was achieved in a sample with a density of 73.7%.
3. Comparatively, for a fixed hatch distance, the scanning speed had a stronger effect than the laser power in the resulting amorphous fraction. The origin of the potent effect of v lies in its stronger influence on the melt pool size and, in turn, on the corresponding HAZ volume.
4. The saturation magnetization and the coercive field of the LPBF processed samples are both inversely related to the amorphous fraction, albeit the influence of the latter is much stronger in H_c. In comparison with a fully amorphous ribbon of the same composition the saturation magnetization obtained in printed samples is slightly larger due to the presence of crystalline phases, but the lowest coercivity achieved is still three orders of magnitude larger.
5. The preferential paths for crack propagation lie perpendicular to crystalline/amorphous interfaces. Thus, altering the geometry of and spatial distribution of melt pools, and consequently of the associated HAZs, might constitute a useful tool to design crack networks leading to higher resistance to eddy currents and, in turn, to lower energy losses.

CRediT authorship contribution statement

M. Rodríguez-Sánchez: Writing – original draft, Visualization, Methodology, Investigation, Formal analysis. **S. Sadanand:** Validation. **A. Ghavimi:** Validation, Investigation. **R. Busch:** Supervision, Methodology, Funding acquisition. **P. Tiberto:** Writing – review & editing, Supervision, Funding acquisition. **E. Ferrara:** Methodology. **G. Barrera:** Investigation, Formal analysis. **L. Thorsson:** Validation, Funding acquisition. **H.J. Wachter:** Validation. **I. Gallino:** Supervision, Project administration, Funding acquisition. **M.T. Pérez-Prado:** Writing – review & editing, Supervision, Funding acquisition, Conceptualization.

Declaration of competing interest

The authors declare that they have no known competing financial interests or personal relationships that could have appeared to influence the work reported in this paper.

Acknowledgments

The work hereby presented has been carried out under the scope AM2SoftMag project, funded by the European Innovation Council through the HORIZON-EIC-2021-PATHFINDEROPEN-01 grant (GA: 101046870). The authors thank the rest of the AM2SoftMag partners for their involvement in the project. Extended acknowledgement is given to Amalia San Román and Ignacio Escobar for their assistance with LPBF trials, to Javier García Molleja for his support with XRD measurements, to Maryam Rahimi Chegeni for her upholding in calorimetry measurements, and to Sergi Bafaluy and María Dolores Martín for their guidance with image analysis procedures.

Supplementary materials

Supplementary material associated with this article can be found, in the online version, at doi:10.1016/j.mtla.2024.102111.

References

[1] B.D. Cullity, C.D. Graham, Introduction to Magnetic Materials, 2nd ed., 2008. Hoboken, New Jersey.
[2] P. Tiberto, M. Baricco, E. Olivetti, R. Piccin, Magnetic properties of bulk metallic glasses, Adv. Eng. Mater. 9 (2007) 468–474.
[3] G. Herzer, Modern soft magnets: amorphous and nanocrystalline materials, Acta Mater. 61 (2013) 718–734.
[4] C. Suryanarayana, A. Inoue, Iron-based bulk metallic glasses, Int. Mater. Rev. 58 (2013) 131–166.
[5] H. Liebermann, C. Graham, Production of amorphous alloy ribbons and effects of apparatus parameters on ribbon dimensions, IEEE Trans. Magn. 12 (1976) 921–923.
[6] J. Shen, Q. Chen, J. Sun, H. Fan, G. Wang, Exceptionally high glass-forming ability of an FeCoCrMoCBY alloy, Appl. Phys. Lett. 86 (2005) 151907.
[7] M. Nabiałek, Soft magnetic and microstructural investigation in Fe-based amorphous, J. Alloys Compd. 642 (2015) 98–103.
[8] I. Otsuka, K. Wada, Y. Maeta, T. Kadomura, M. Yagi, Magnetic properties of Fe-based amorphous powders with high-saturation induction produced by spinning water atomization process (SWAP), IEEE Trans. Magn. 44 (2008) 3891–3894.
[9] A. Hussein, L. Hao, C. Yan, R. Everson, Finite element simulation of the temperature and stress fields in single layers built without-support in selective laser melting, Mater. Des. 52 (2013) 638–647.
[10] T. DebRoy, H.L. Wei, J.S. Zuback, T. Mukherjee, J.W. Elmer, J.O. Milewski, A. M. Beese, A. Wilson-Heid, A. De, W. Zhang, Additive manufacturing of metallic components – Process, structure and properties, Prog. Mater. Sci. 92 (2018) 112–224.
[11] S. Ramadurga Narasimharaju, W. Zeng, T. Long See, Z. Zhu, P. Scott, X. Jiang, S. Lou, A comprehensive review on laser powder bed fusion of steels: processing, microstructure, defects and control methods, mechanical properties, current challenges and future trends, J. Manuf. Process. 75 (2022) 375–414.
[12] J. Wang, R. Zhu, Y. Liu, L. Zhang, Understanding melt pool characteristics in laser powder bed fusion: an overview of single-and multi-track melt pools for process optimization, Adv. Powder Mater. 2 (2023) 100137.
[13] H.X. Li, Z.C. Lu, S.L. Wang, Y. Wu, Z.P. Lu, Fe-based bulk metallic glasses: glass formation, fabrication, properties and applications, Prog. Mater. Sci. 103 (2019) 235–318.
[14] H. Liu, Q. Jiang, J. Huo, Y. Zhang, W. Yang, X. Li, Crystallization in additive manufacturing of metallic glasses: a review, Addit. Manuf. 36 (2020) 101568.
[15] Q. Halim, N.A.N. Mohamed, M.R.M. Rejab, W.N.W.A. Naim, Q. Ma, Metallic glass properties, processing method and development perspective: a review, Int. J. Adv. Manuf. Technol. 112 (2021) 1231–1258.
[16] N. Sohrabi, J. Jhabvala, R.E. Logé, Additive manufacturing of bulk metallic glasses—process, challenges and properties: a review, Met 11 (2021) 1279.
[17] C. Zhang, D. Ouyang, S. Pauly, L. Liu, 3D printing of bulk metallic glasses, Mater. Sci. Eng. R Rep. 145 (2021) 100625.
[18] P. Zhang, J. Tan, Y. Tian, H. Yan, Z. Yu, Research progress on selective laser melting (SLM) of bulk metallic glasses (BMGs): a review, Int. J. Adv. Manuf. Technol. 118 (2021) 2017–2057.
[19] H.R. Lashgari, M. Ferry, S. Li, Additive manufacturing of bulk metallic glasses: fundamental principle, current/future developments and applications, J. Mater. Sci. Technol. 119 (2022) 131–149.
[20] A. Mostafaei, C. Zhao, Y. He, S.Reza Ghiaasiaan, B. Shi, S. Shao, N. Shamsaei, Z. Wu, N. Kouraytem, T. Sun, J. Pauza, J.V. Gordon, B. Webler, N.D. Parab, M. Asherloo, Q. Guo, L. Chen, A.D. Rollett, Defects and anomalies in powder bed fusion metal additive manufacturing, Curr. Opin. Solid State Mater. Sci. 26 (2022) 100974.
[21] D. Ouyang, W. Xing, N. Li, Y. Li, L. Liu, Structural evolutions in 3D-printed Fe-based metallic glass fabricated by selective laser melting, Addit. Manuf. 23 (2018) 246–252.
[22] Ł. Żrodowski, R. Wróblewski, M. Leonowicz, B.M. Morończyk, T. Choma, J. Ciftci, W.Wojciech Święszkowski, A. Dobkowska, E. Ura-Bińczyk, P. Błyskun, P. Błyskun, J. Jaroszewicz, A. Krawczyńska, K. Kulikowski, B. Wysocki, T. Cetner, G. Moneta, X. Li, L. Yuan, A. Małachowska, P.J. Masset, R. Chulist, C. Żrodowski, How to control the crystallization of metallic glasses during laser powder bed fusion? Towards part-specific 3D printing of in situ composites, Addit. Manuf. 76 (2023) 103775.
[23] X.P. Li, M.P. Roberts, S. O'Keeffe, T.B. Sercombe, Selective laser melting of Zr-based bulk metallic glasses: processing, microstructure and mechanical properties, Mater. Des. 112 (2016) 217–226.

[24] C. Zhang, X. Li, S.Q. Liu, H. Liu, L.J. Yu, L. Liu, 3D printing of Zr-based bulk metallic glasses and components for potential biomedical applications, J. Alloys Compd. 790 (2019) 963–973.
[25] J.J. Marattukalam, V. Pacheco, D. Karlsson, L. Riekehr, J. Lindwall, F. Forsberg, U. Jansson, M. Sahlberg, B. Hjörvarsson, Development of process parameters for selective laser melting of a Zr-based bulk metallic glass, Addit. Manuf. 33 (2020) 101124.
[26] J. Wegner, M. Frey, S. Kleszczynski, R. Busch, G. Witt, Influence of process gas during powder bed fusion with laser beam of Zr-based bulk metallic glasses, Procedia CIRP 94 (2020) 205–210.
[27] N. Sohrabi, J. Jhabvala, G. Kurtuldu, M. Stoica, A. Parrilli, S. Berns, E. Polatidis, S. Van Petegem, S. Hugon, A. Neels, J.F. Löffler, R.E. Logé, Characterization, mechanical properties and dimensional accuracy of a Zr-based bulk metallic glass manufactured via laser powder-bed fusion, Mater. Des. 199 (2021) 109400.
[28] H.Y. Jung, S.J. Choi, K.G. Prashanth, M. Stoica, S. Scudino, S. Yi, U. Kühn, D. H. Kim, K.B. Kim, J. Eckert, Fabrication of Fe-based bulk metallic glass by selective laser melting: a parameter study, Mater. Des. 86 (2015) 703–708.
[29] Y. Zhang, B. Song, L. Zhang, Z. Wang, Y. Shi, Microstructure and crack distribution of Fe-based amorphous alloys manufactured by selective laser melting, in: 2017 International Solid Freeform Fabr. Symposium, 2017.
[30] Z. Mahbooba, L. Thorsson, M. Unosson, P. Skoglund, H. West, T. Horn, C. Rock, E. Vogli, O. Harrysson, Additive manufacturing of an iron-based bulk metallic glass larger than the critical casting thickness, Appl. Mater. Today. 11 (2018) 264–269.
[31] W. Xing, D. Ouyang, N. Li, L. Liu, Insight into micro-cracking in 3D-printed Fe-based BMGs by selective laser melting, Intermetallics 103 (2018) 101–106.
[32] N. Li, J. Zhang, W. Xing, D. Ouyang, L. Liu, 3D printing of Fe-based bulk metallic glass composites with combined high strength and fracture toughness, Mater. Des. 143 (2018) 285–296.
[33] X.D. Nong, X.L. Zhou, Y.X. Ren, Fabrication and characterization of Fe-based metallic glasses by selective laser melting, Opt. Laser Technol. 109 (2019) 20–26.
[34] L. Wang, H. Wang, Y. Liu, Z. Fu, T. Peng, J. Shen, S. Zhou, M. Yan, G. Wang, Y. Dai, Selective laser melting helps fabricate record-large bulk metallic glass: experiments, simulation and demonstrative part, J. Alloys Compd. 808 (2019) 151731.
[35] F. Xie, Q. Chen, J. Gao, Brittle-ductile transition in laser 3D printing of Fe-based bulk metallic glass composites, Met 9 (2019) 78.
[36] F. Xie, Q. Chen, J. Gao, Y. Li, Laser 3D printing of Fe-based bulk metallic glass: microstructure evolution and crack propagation, J. Mater. Eng. Perform. 28 (2019) 3478–3486.
[37] S.X. Liang, X. Wang, W. Zhang, Y.J. Liu, W. Wang, L.C. Zhang, Selective laser melting manufactured porous Fe-based metallic glass matrix composite with remarkable catalytic activity and reusability, Appl. Mater. Today. 19 (2020) 100543.
[38] N. Luo, C. Scheitler, N. Ciftci, F. Galgon, Z. Fu, V. Uhlenwinkel, M. Schmidt, C. Körner, Preparation of Fe-Co-B-Si-Nb bulk metallic glasses by laser powder bed fusion: microstructure and properties, Mater. Charact. 162 (2020) 110206.
[39] Y.M. Zou, Y.S. Wu, K.F. Li, C.L. Tan, Z.G. Qiu, D.C. Zeng, Selective laser melting of crack-free Fe-based bulk metallic glass via chessboard scanning strategy, Mater. Lett. 272 (2020) 127824.
[40] Y. Zou, Z. Qiu, C. Tan, Y. Wu, K. Li, D. Zeng, Microstructure and mechanical properties of Fe-based bulk metallic glass composites fabricated by selective laser melting, J. Non Cryst. Solids. 538 (2020) 120046.
[41] Y. Zou, Z. Qiu, Z. Zheng, G. Wang, X. Yan, S. Yin, M. Liu, D. Zeng, Ex-situ additively manufactured FeCrMoCB/Cu bulk metallic glass composite with well wear resistance, Tribol. Int. 162 (2021) 107112.
[42] S. Gao, X. Yan, C. Chang, E. Aubry, P. He, M. Liu, H. Liao, N. Fenineche, Microstructure and magnetic properties of FeSiBCrC soft magnetic alloy manufactured by selective laser melting, Mater. Lett. 290 (2021) 129469.
[43] N. Li, S. Wu, D. Ouyang, J. Zhang, L. Liu, Fe-based metallic glass reinforced FeCoCrNiMn high entropy alloy through selective laser melting, J. Alloys Compd. 822 (2020) 153695.
[44] Q. Jiang, P. Zhang, J. Tan, Z. Yu, Y. Tian, S. Ma, D. Wu, Influence of the microstructure on mechanical properties of SLM additive manufacturing Fe-based bulk metallic glasses, J. Alloys Compd. 894 (2022) 162525.
[45] M.G. Özden, N.A. Morley, Optimizing laser additive manufacturing process for Fe-based nano-crystalline magnetic materials, J. Alloys Compd. 960 (2023) 170644.
[46] S. Pauly, L. Lö Ber, R. Petters, M. Stoica, S. Scudino, U. Kü Hn, J. Rgen Eckert, Processing metallic glasses by selective laser melting, Mater. Today. 16 (2013) 37–41.
[47] Ł. Żrodowski, B. Wysocki, R. Wróblewski, K.J. Kurzydłowski, W. Święszkowski, The novel scanning strategy for fabrication metallic glasses by selective laser melting, Laser 20 (2016) 20.
[48] Ł. Żrodowski, B. Wysocki, R. Wróblewski, A. Krawczyńska, B. Adamczyk-Cieślak, J. Zdunek, P. Błyskun, J. Ferenc, M. Leonowicz, W. Święszkowski, New approach to amorphization of alloys with low glass forming ability via selective laser melting, J. Alloys Compd. 771 (2019) 769–776.
[49] Y.G. Nam, B. Koo, M.S. Chang, S. Yang, J. Yu, Y.H. Park, J.W. Jeong, Selective laser melting vitrification of amorphous soft magnetic alloys with help of double-scanning-induced compositional homogeneity, Mater. Lett. 261 (2020) 127068.
[50] L. Thorsson, M. Unosson, M.Teresa Pérez-Prado, X. Jin, P. Tiberto, G. Barrera, B. Adam, N. Neuber, A. Ghavimi, M. Frey, R. Busch, I. Gallino, Selective laser melting of a Fe-Si-Cr-B-C-based complex-shaped amorphous soft-magnetic electric motor rotor with record dimensions, Mater. Des. 215 (2022) 110483.
[51] ASTM International, Standard test methods for flow rate of metal powders using the hall flowmeter funnel, in: ASTM Standard, 2016.
[52] ASTM B527-20, ASTM B527-20 standard test method for tap density of metal powders and compounds, in: ASTM International, 2020.
[53] M.A. Kaleem, M.Z. Alam, M. Khan, S.H.I. Jaffery, B. Rashid, An experimental investigation on accuracy of Hausner Ratio and Carr Index of powders in additive manufacturing processes, Met. Powder Rep. 76 (2021) 50–54.
[54] H. Ghasemi-Tabasi, J. Jhabvala, E. Boillat, T. Ivas, R. Drissi-Daoudi, R.E. Logé, An effective rule for translating optimal selective laser melting processing parameters from one material to another, Addit. Manuf. 36 (2020) 101496.
[55] A.D. Goodall, L. Chechik, R.L. Mitchell, G.W. Jewell, I. Todd, Cracking of soft magnetic FeSi to reduce eddy current losses in stator cores, Addit. Manuf. 70 (2023) 103555.
[56] I. Rodríguez-Barber, A.M. Fernández-Blanco, I. Unanue-Arruti, I. Madariaga-Rodríguez, S. Milenkovic, M.T. Pérez-Prado, Laser powder bed fusion of the Ni superalloy Inconel 939 using pulsed wave emission, Mater. Sci. Eng. A. 870 (2023) 144864.
[57] I. Arganda-Carreras, V. Kaynig, C. Rueden, K.W. Eliceiri, J. Schindelin, A. Cardona, H.S. Seung, Trainable Weka Segmentation: a machine learning tool for microscopy pixel classification, Bioinform 33 (2017) 2424–2426.
[58] A. Załuska, H. Matyja, Crystallization characteristics of amorphous Fe-Si-B alloys, J. Mater. Sci. 18 (1983) 2163–2172.
[59] D.S. Dos Santos, D.R. Dos Santos, Crystallization kinetics of Fe-B-Si metallic glasses, J. Non Cryst. Solids. 304 (2002) 56–63.
[60] P. Gorria, I. Orue, F. Plazaola, M. Fernandez-Gubieda, J. Barandiaran, Magnetic and Mossbauer study of amorphous and nanocrystalline Fe/sub 86/Zr/sub 7/Cu/sub 1/B/sub 6/alloys, IEEE Trans. Magn. 29 (1993) 2682–2684.
[61] T.V. Eagar, N.S. Tsai, Temperature fields produced by traveling distributed heat sources, Weld. J. 62 (1983) 346–355.
[62] T. Qi, H. Zhu, H. Zhang, J. Yin, L. Ke, X. Zeng, Selective laser melting of Al7050 powder: melting mode transition and comparison of the characteristics between the keyhole and conduction mode, Mater. Des. 135 (2017) 257–266.
[63] M. Markl, C. Körner, Multiscale modeling of powder bed–based additive manufacturing, Annu. Rev. Mater. 46 (2016) 93–123.
[64] R. Cunningham, C. Zhao, N. Parab, C. Kantzos, J. Pauza, K. Fezzaa, T. Sun, A. D. Rollett, Keyhole threshold and morphology in laser melting revealed by ultrahigh-speed x-ray imaging, Sci 363 (2019) 849–852.
[65] R. Rai, J.W. Elmer, T.A. Palmer, T. Debroy, Heat transfer and fluid flow during keyhole mode laser welding of tantalum, Ti–6Al–4V, 304L stainless steel and vanadium, J. Phys. D Appl. Phys. 40 (2007) 5753.
[66] R. Drissi-Daoudi, G. Masinelli, C. de Formanoir, K. Wasmer, J. Jhabvala, R.E. Logé, Acoustic emission for the prediction of processing regimes in Laser Powder Bed Fusion, and the generation of processing maps, Addit. Manuf. 67 (2023) 103484.
[67] L.E. Criales, Y.M. Arısoy, B. Lane, S. Moylan, A. Donmez, T. Özel, Laser powder bed fusion of nickel alloy 625: experimental investigations of effects of process parameters on melt pool size and shape with spatter analysis, Int. J. Mach. Tools Manuf. 121 (2017) 22–36.
[68] M. Afrasiabi, D. Keller, C. Lüthi, M. Bambach, K. Wegener, Effect of process parameters on melt pool geometry in laser powder bed fusion of metals: a numerical investigation, Procedia CIRP 113 (2022) 378–384.
[69] Q. Guo, C. Zhao, M. Qu, L. Xiong, L.I. Escano, S.M.H. Hojjatzadeh, N.D. Parab, K. Fezzaa, W. Everhart, T. Sun, L. Chen, In-situ characterization and quantification of melt pool variation under constant input energy density in laser powder bed fusion additive manufacturing process, Addit. Manuf. 28 (2019) 600–609.
[70] P. Akbari, F. Ogoke, N.Y. Kao, K. Meidani, C.Y. Yeh, W. Lee, A. Barati Farimani, MeltpoolNet: melt pool characteristic prediction in metal additive manufacturing using machine learning, Addit. Manuf. 55 (2022) 102817.
[71] W.E. King, H.D. Barth, V.M. Castillo, G.F. Gallegos, J.W. Gibbs, D.E. Hahn, C. Kamath, A.M. Rubenchik, Observation of keyhole-mode laser melting in laser powder-bed fusion additive manufacturing, J. Mater. Process. Technol. 214 (2014) 2915–2925.
[72] J.J.S. Dilip, S. Zhang, C. Teng, K. Zeng, C. Robinson, D. Pal, B. Stucker, Influence of processing parameters on the evolution of melt pool, porosity, and microstructures in Ti-6Al-4V alloy parts fabricated by selective laser melting, Prog. Addit. Manuf. 2 (2017) 157–167.
[73] A. Keshavarzkermani, E. Marzbanrad, R. Esmaeilizadeh, Y. Mahmoodkhani, U. Ali, P.D. Enrique, N.Y. Zhou, A. Bonakdar, E. Toyserkani, An investigation into the effect of process parameters on melt pool geometry, cell spacing, and grain refinement during laser powder bed fusion, Opt. Laser Technol. 116 (2019) 83–91.
[74] J. Metelkova, Y. Kinds, K. Kempen, C. de Formanoir, A. Witvrouw, B. Van Hooreweder, On the influence of laser defocusing in Selective Laser Melting of 316L, Addit. Manuf. 23 (2018) 161–169.